Recent Developments in Measurement and Tracking of the APS Storage Ring Beam Emittance

Bingxin Yang, Alex H. Lumpkin,
Louis Emery, and Michael Borland

Advanced Photon Source, Argonne National Laboratory,
9700 South Cass Avenue, Argonne, IL 60565

Abstract. The x-ray pinhole camera is used at the APS storage ring to measure the beam emittance. The measured data are archived during user operation. At 1 Hz bandwidth, we have achieved better than 1 μm stability in the measured horizontal beam size, typically of 143 μm, corresponding to 8 nm·rad. During user runs, beam size variations up to 2.5 μm were observed (corresponding to emittance variations of 0.4 nm·rad), which were strongly correlated and attributed to the variation of electron energy loss in the insertion devices. In other words, the user-initiated insertion device gap changes are the major factor in observed beam emittance variations during user runs.

INTRODUCTION

Pinhole cameras have been successfully used for measurements of accelerator beam sizes in the past several years [1-4]. The short and long-term stability of the measurements is affected by many instrumental and environmental factors. In this work, we present our progress in stabilizing the performance of the x-ray pinhole camera at the Advanced Photon Source (APS) storage ring. At high resolution (σ_{res} = 22 μm) and good stability (within 1 μm over weeks), we show that the insertion device gap change by the users is the dominant factor for emittance variations during user runs.

EXPERIMENT

The basic components of the pinhole camera are listed in Table 1. A water-cooled small aperture is used first to limit the power load on the pinhole. Two sets of tungsten

CP546, *Beam Instrumentation Workshop 2000*, edited by Kenneth D. Jacobs and R. Coles Sibley III
2000 American Institute of Physics 1-56396-975-0

slits, in horizontal and vertical directions, form the imaging pinhole. A thin YAG scintillator screen is used to convert the x-ray image into a visible one at peak wavelength of 530 nm. A pair of achromat lenses produces a 1:2 magnified image at a SONY XC-75 CCD camera. An aperture wheel is inserted between the two lenses for intensity control. The intensity, focus and the x, y position of the image can be remotely adjusted.

The video signal is transported through a combination of copper and optical fiber cables and digitized by a VME image grabber Datacube MV-200. The images are converted to integrated x- and y-profiles, averaged over a specified time interval, and fitted to Gaussian functions. The fitted peak parameters are then archived at one-minute intervals by the APS data-logger system.

TABLE 1. Parameters of the Pinhole Camera.

Component	Location	Notes
Small aperture	8.7 m from the source	Water-cooled, 0.5 mm diameter hole
Pinhole slits	8.867 m from the source	Water-cooled, 0 - 100 μm adjustable
YAG screen	16.713 m from the source	80 μm thick
Lens No. 1	200 mm from YAG screen	Achromat with 200 mm focal length
Aperture wheel	Between 2 lenses	Aperture of 12, 20, 25, 32, and 50 mm
Lens No. 2	350 mm from Lens No. 1	Achromat with 400 mm focal length
Camera	400 mm from Lens No. 2	SONY XC-75 1/2" CCD camera

Optimization of the Pinhole Camera

To reduce the effect of small-angle scattering from the vacuum windows and to maintain chemical stability of the pinhole slits, it is necessary to maintain a vacuum optical path. The slits are made of 6 mm thick tungsten (99.5% pure), and its optical edge is made of cylindrical surfaces of 50 mm radii. The cylindrical surface makes the optical thickness vary with the transverse coordinate into the blade (Figure 1). It can be seen that the edge is defined to better than 1 μm for x-ray energies most useful to us. The cylindrical shape allows for up to ±2° misalignment of the blades, which greatly simplifies their accuracy requirements for design, fabrication and positioning.

The independent blades allow for accurate setting of slit width. First the total x-ray flux through the slits is measured as we scan the slit width. Below 2 μm, the leakage through blade defects and multiple scattering backgrounds are important, the flux curve is not a linear function of the slit setting. Above 2 μm, the curve is a straight line and the effective zero-slits offset can be obtained by extrapolating it to zero-flux (Figure 1B). It is important to note that the normal slits setting of 20 μm is well above the nonlinear portion of the curve.

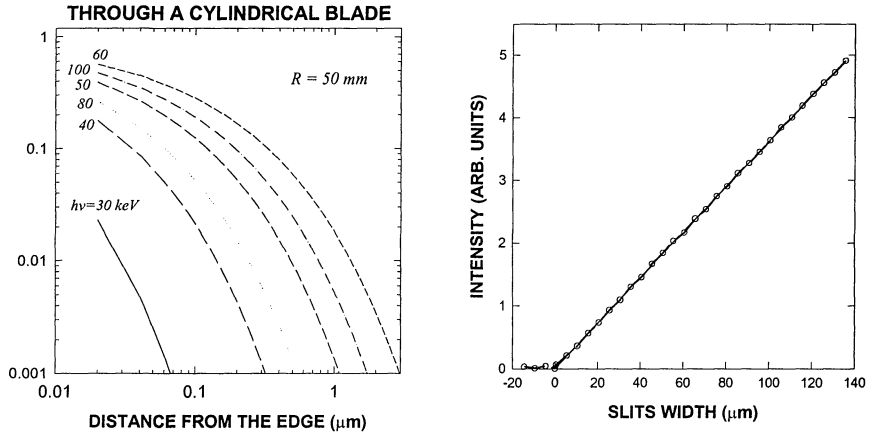

FIGURE 1. (A: Left) Transmission of x rays, with photon energies from 30 to 100 keV, through a cylindrical tungsten blade as a function of distance from the edge surface. (B: Right) Measured total transmitted x-ray flux intensity as a function of slits width. This quasilinear dependence is used to calibrate the slit width.

This design also makes the slit width sensitive to the blade temperatures. When the blades are cooled by airflow, the temperature rises more than 10° C for 100 mA of electron beam and the thermal expansion of the components reduces the slit width by several micrometers. A strong evidence of the slits closing is shown by the decrease in observed peak counts per mA-current at high current (Figure 2A). We used water cooling to stabilize the temperature of the slit components, stabilizing the beam size measurement to within 0.4 μm over a 25 minute interval (Figure 2B). Further upgrade of the temperature control system in 1999 brought the water temperature regulation to within ±0.05° C (Figure 2C), and the measured beam size fluctuation decreased further.

The x-ray image of the pinhole camera was converted into a visible light image with an ultrathin YAG scintillator (80 μm thick), used to reduce image-blurring due to multiple scattering and depth-of-source effect. The imaging optics used two achromat lenses, each focused at infinity (infinite conjugate). In this arrangement, the intensity control apertures / filters can be conveniently inserted with minimum effect on the focusing distance. Neutral density filters were used initially but were found to be less than satisfactory: some filters have cylindrically curved surfaces, causing the x and y focus to differ more than one expects from beam size asymmetry; some filters have a tapered thickness, shifting the beam spot about when intensity adjustments are made. Fixed apertures were found to be more reliable than the commercial quality ND filters.

The calibration of camera scales was performed with a back-illuminated grid of pinholes in close contact with the translucent YAG screen. During the calibration, a Gaussian fit yields the center coordinates of the pinhole with an estimated accuracy of 0.5 pixels or better. The entire grid, normally containing 6 to 9 pinholes in the video

screen, is fitted to the periodic lattice to obtain the x- and y- calibration, as well as the tilt angle. The rms deviation of the measured centroid coordinates was found to be less than 0.5% of the grid spacing.

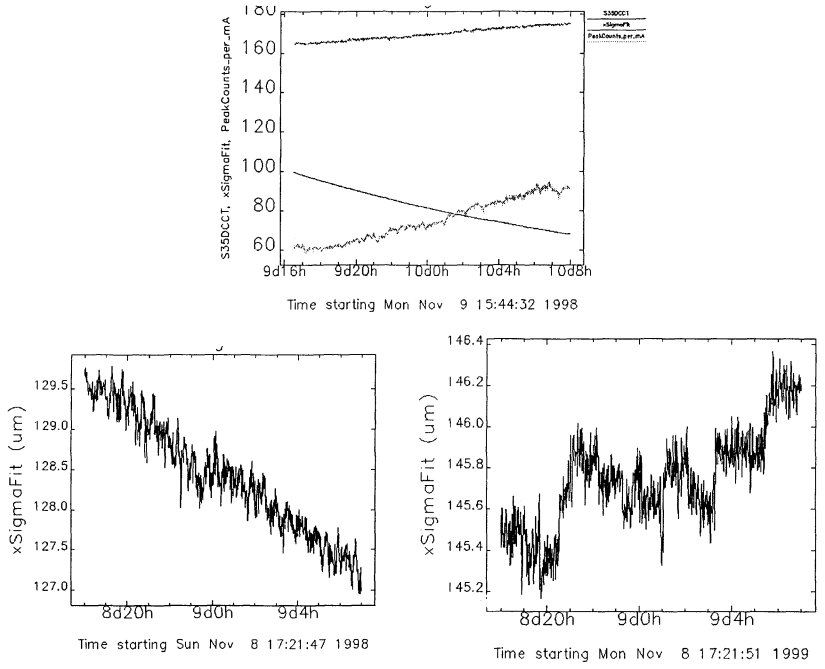

FIGURE 2. Measured vertical beam sizes show significant correlation with the slits temperature. (A: Upper) air-cooled slits in AM-line, the top curve, note that the decaying beam current, and the size / current ratio are also shown. (B: Lower-left) Water-cooled slits in BM-line, temperature regulated to ±0.25°C; (C: Lower-right) Water-cooled slits, temperature regulated to ±0.05° C. Note different vertical scales of the lower plots.

To obtain good stability, a low-noise video transport and digitization, as well as a robust data processing algorithm is crucial. At the time of writing, averaging over fifteen consecutive frames of video data (approximately 0.5 seconds) is still necessary to achieve good signal-to-noise ratio. To save storage space, the average of the profiles are performed with the following algorithm,

$$[F(x)]_{NEW} = \frac{W-1}{W}[F(x)]_{Old} + \frac{1}{W}[F(x)]_{Single\_Frame}, \qquad (1)$$

where W is the number of frames to average.

Several approaches of background removal were tested. Some frame-grabber manufacturers recommend setting the digitizer offset to be slightly negative to reduce the background noise. This approach underestimates the photon flux and has two detrimental consequences: The measured beam size is systematically smaller than the actual one and changes with light intensity, i.e., with beam current or light attenuators. Since the video data is always positive, subtracting a background video frame (taken without x-ray beam) has a subtle effect similar to a negative offset. To avoid these problems, we actually set the digitizer offset to be slightly positive, so that the fluctuations of the analog background do not make the digitizer cross zero. The background is calculated from the averaged profile data far away from the peak and then subtracted with a straight-line interpolation (Fig. 3).

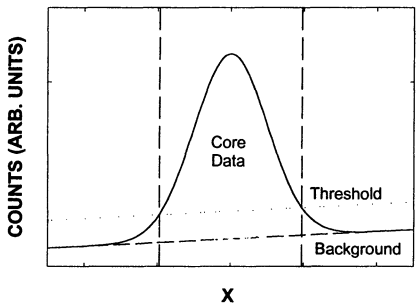

FIGURE 3. Illustration of the algorithm for background removal and selection of the core data. In this example, only data points above 15% of the maximum value are used for calculating peak width and area.

To make sure that the VME processor (IOC) processes the data at the full video rate, we chose to use linear algorithms and only apply them to the core of the beam, namely, only to the data points above a given threshold,

$$(x,F)=\left\{(x,f)\big|_{f>af_{max}}\right\}, \tag{2}$$

where f_{max} is the maximum value of the profile data f, and a is the threshold ratio, usually chosen to be higher than the noise level under normal operating conditions.

In the first approach (rms calculation), the total area A' and rms width σ' are first calculated from the subset defined by Eq. (2). The width of an equivalent Gaussian peak is obtained by multiplying σ' by a correction factor,

$$C_\sigma=\left\{\int_{-\sqrt{-2\ln a}}^{\sqrt{-2\ln a}}e^{-x^2/2}dx\Big/\int_{-\sqrt{-2\ln a}}^{\sqrt{-2\ln a}}x^2e^{-x^2/2}dx\right\}^{1/2} \tag{3}$$

For a Gaussian peak, this correction would recover the true rms width, making it independent of the threshold ratio a. The area of the equivalent Gaussian peak can be obtained similarly by multiplying A' by the correction factor,

$$C_A = \left\{ \int_{-\sqrt{-2\ln a}}^{\sqrt{-2\ln a}} e^{-x^2/2} dx \right\}^{-1/2}. \tag{4}$$

In the second approach, the logarithm of the profile in the subset data is fitted to a quadratic form to obtain the equivalent Gaussian peak parameters,

$$\ln F(x) \to \ln P - \frac{(x - x_0)^2}{2\sigma^2}. \tag{5}$$

Using these fast algorithms, the IOC runs at half frame rate (15 frames/second) for a full screen data, or at full frame rate (30 frame/second) for a smaller region of interest. Figure 4 shows an example of calculated peak width from these two different algorithms. They are very similar under normal operating conditions. The peak width derived from the fit appears to be slightly more stable.

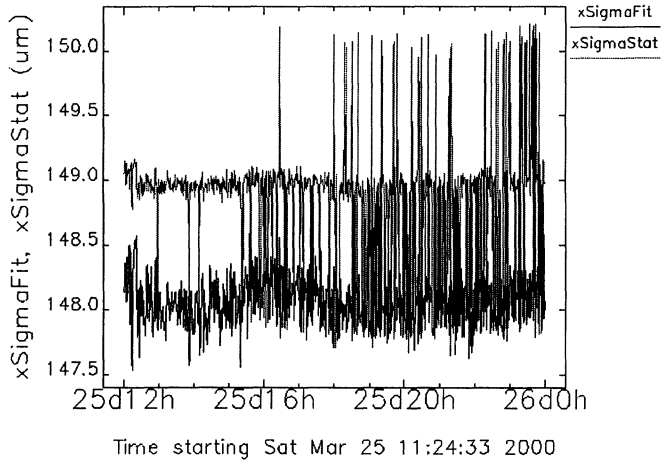

FIGURE 4. A random sample of peak width from the APS data logger over a 12 hour period. Top (xSigmaStat): horizontal beam size derived from the rms calculations. Bottom (xSigmaFit): the horizontal beam size derived from the Gaussian fit.

PERFORMANCE

The resolution of the pinhole camera is derived from the lifetime dependence on the beam size. We assume that the measured vertical beam size is the quadrature sum of the camera resolution and the true beam size,

$$\sigma_{exp}^2 = \sigma_R^2 + \sigma_y^2. \tag{6}$$

The rate of the beam loss in the ring can be written as the sum of two processes, electrons scattering with the gas molecules and with each other (Touschek scattering),

$$\frac{1}{\tau} = A_1 I + A_2' \frac{I}{bunch\_volume} \cong A_2 \frac{I^{2/3}}{\sigma_y}, \tag{7}$$

where A_1 and A_2 are proportional constants. The second step used the fact that the bunch length is proportional to $I^{1/3}$, and Touschek loss dominates at high bunch current. We measured the beam lifetime and beam size for high-bunch current, 2.5 mA, while varying the vertical coupling. After fitting the data to the above expressions (Figure 5), the zero-lifetime limit gives the total resolution σ_R of 22 μm. This value agrees with that estimated by a broadband Fresnel diffraction model [4] within 10%.

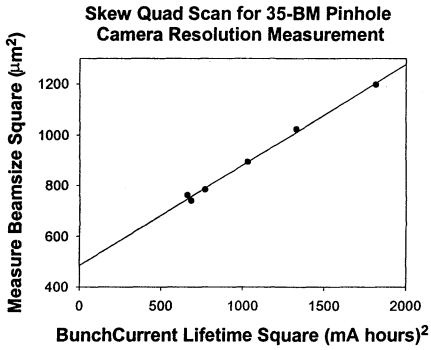

FIGURE 5. Resolution characterization with lifetime measurement vs. vertical beam size. Extrapolation to the zero lifetime, with known lifetime-beam size dependence, gives the total camera resolution of 22 μm.

Figure 6 shows the archived beam size data over a three week period. The high-frequency variations of the measured beam size are less than 1 μm (width of the dark band), at 1 Hz bandwidth. During user runs, the beam size can vary up to 2.5 μm. To examine the origin of these variations, we zoom in the first two weeks and then in the first two days. Figure 7 plots the horizontal emittance and the total energy loss in all

APS insertion devices and shows strong (anti) correlation between the two quantities. A quantitative analysis yields a correlation coefficient of -0.74 ± 0.01 for the two quantities over these periods. We thus conclude that beam size variation in the APS beam (1.4% in BM, 3% in ID) is largely due to the insertion device gap changes initiated by the users.

CONCLUSION

Significant effort has been made to improve the stability and reliability of the APS pinhole camera for emittance measurements. At 1 Hz bandwidth, we have achieved better than 1 μm stability in the measured horizontal beam size, typically of 143 μm. During user runs, the APS storage ring horizontal beam size at the bending magnet is normally stable within a 2 μm range (1.4%), equivalent to a 3% beam size change at the insertion devices. The variations of horizontal beam size and emittance are induced mainly by insertion device gap changes initiated by users. Current upgrade efforts for the system are concentrated on reducing the video noise and broadening the bandwidth of measurements.

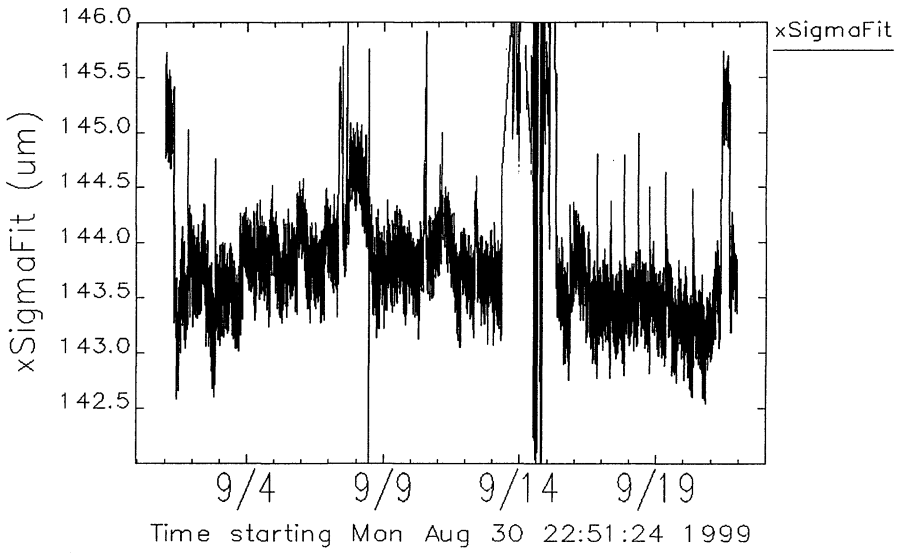

FIGURE 6. The rms horizontal beam size (measured at 1 Hz bandwidth, recorded at 1 minute interval) during September 1999 recorded by the APS data logger. Significant variations can be seen during machine studies on September 1, 7, 14-15, and 21.

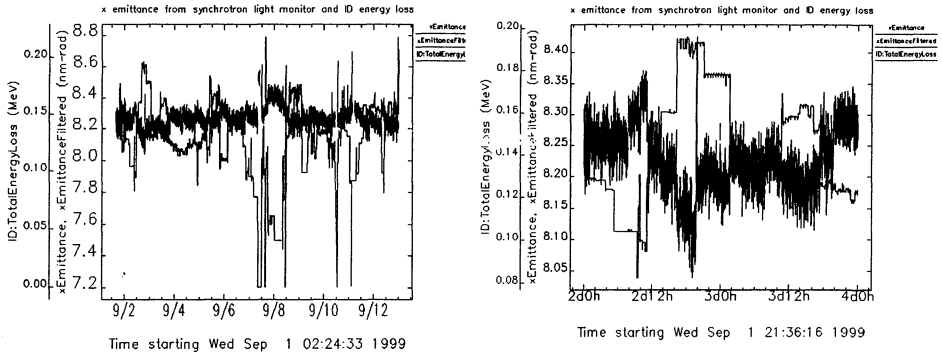

FIGURE 7. The horizontal beam emittance in the first two weeks (A) and first two days (B) during September 1999 recorded by the APS data logger. The total energy loss in the APS insertion devices is also plotted (thin lines).

ACKNOWLEDGMENTS

We would like to thank Ned Arnold and Frank Lenkszus for their support in the beamline controls, and R. Dortwegt for water temperature regulation. We would like to also acknowledge J. Galayda and G. Decker for their foresight and strong support of the diagnostics beamline project. This work was supported by the U.S. Department of Energy, Office of Basic Energy Sciences, under Contract No. W-31-109-ENG-38.

REFERENCES

1. Elleaume, P., et al., "Measuring Ultra Small Electron Emittance Using an X-ray Pinhole Camera", *ESRF/MACH* ID 95/25, 1995.
2. Cai, Z., et al., "Beam size measurement of the stored electron beam at the APS storage ring using pinhole optics," *Rev. Sci. Instrum.* **67** (9), 3368-3370 (1996).
3. Yang, B. X., and Lumpkin, A., "Particle-Beam Profiling Techniques on the APS Storage Ring," *BIW96, AIP Conf. Proc. 390*, 491-497 (1997).
4. Yang, B. X., and Lumpkin, A., "Simultaneous Measurements of Electron Beam Size and Divergence with an Undulator," *PAC 99,* 2161-2163 (1999).